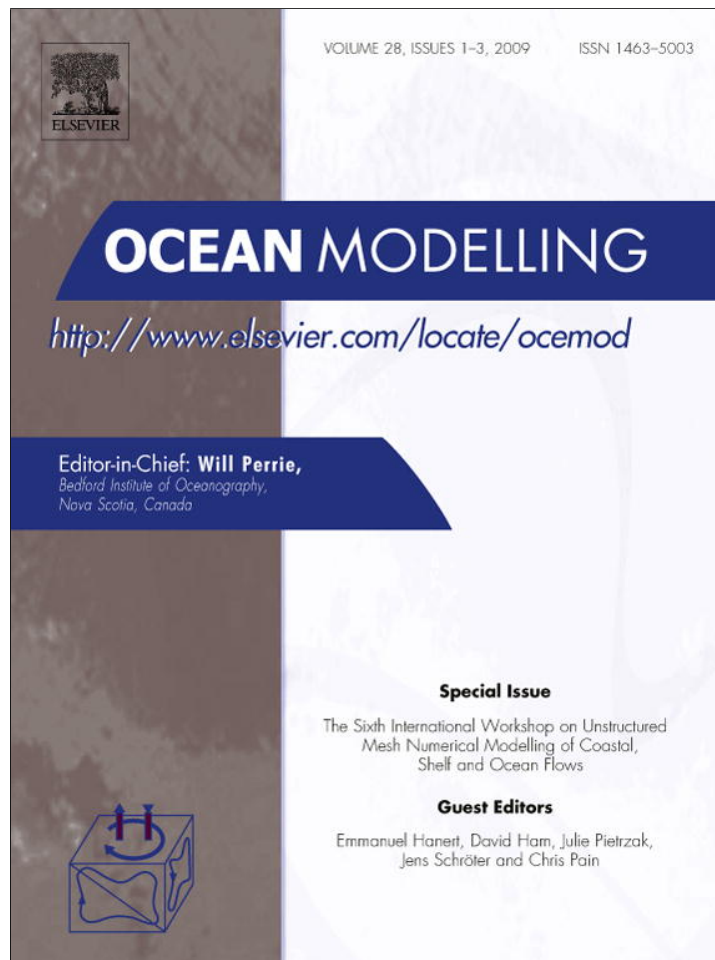


Provided for non-commercial research and education use.
Not for reproduction, distribution or commercial use.



This article appeared in a journal published by Elsevier. The attached copy is furnished to the author for internal non-commercial research and education use, including for instruction at the authors institution and sharing with colleagues.

Other uses, including reproduction and distribution, or selling or licensing copies, or posting to personal, institutional or third party websites are prohibited.

In most cases authors are permitted to post their version of the article (e.g. in Word or Tex form) to their personal website or institutional repository. Authors requiring further information regarding Elsevier's archiving and manuscript policies are encouraged to visit:

<http://www.elsevier.com/copyright>



Contents lists available at ScienceDirect

Ocean Modelling

journal homepage: www.elsevier.com/locate/ocemod

An unstructured-grid finite-volume surface wave model (FVCOM-SWAVE): Implementation, validations and applications

Jianhua Qi^a, Changsheng Chen^{a,d,e,*}, Robert C. Beardsley^b, Will Perrie^c, Geoffrey W. Cowles^a, Zhigang Lai^a

^a Department of Fisheries Oceanography, School for Marine Science and Technology, University of Massachusetts-Dartmouth, 706 South Rodney French Blvd, New Bedford, MA 02744, USA

^b Department of Physical Oceanography, Woods Hole Oceanographic Institution, Woods Hole, MA 02543, USA

^c Fisheries & Oceans Canada, Bedford Institute of Oceanography, Dartmouth, Nova Scotia, Canada

^d Marine Ecosystem and Environmental Laboratory, Shanghai Ocean University, 334 Jungong Road, 200090 Shanghai, PR China

^e The State Key Laboratory for Estuarine and Coastal Research, East China Normal University, Shanghai, PR China

ARTICLE INFO

Article history:

Received 23 April 2008

Received in revised form 25 December 2008

Accepted 13 January 2009

Available online 5 February 2009

Keywords:

Unstructured grid

Finite-volume

Wave model

FVCOM-SWAVE

ABSTRACT

The structured-grid surface wave model SWAN (Simulating Waves Nearshore) has been converted into an unstructured-grid finite-volume version (hereafter referred to as FVCOM-SWAVE) for use in coastal ocean regions with complex irregular geometry. The implementation is made using the Flux-Corrected Transport (FCT) algorithm in frequency space, the implicit Crank–Nicolson method in directional space and options of explicit or implicit second-order upwind finite-volume schemes in geographic space. FVCOM-SWAVE is validated using four idealized benchmark test problems with emphasis on numerical dispersion, wave-current interactions, wave propagation over a varying-bathymetry shallow water region, and the basic wave grow curves. Results demonstrate that in the rectangular geometric domain, the second-order finite-volume method used in FVCOM-SWAVE has the same accuracy as the third-order finite-difference method used in SWAN. FVCOM-SWAVE was then applied to simulate wind-induced surface waves on the US northeast shelf with a central focus in the Gulf of Maine and New England Shelf. Through improved geometric fitting of the complex irregular coastline, FVCOM-SWAVE was able to robustly capture the spatial and temporal variation of surface waves in both deep and shallow regions along the US northeast coast.

Published by Elsevier Ltd.

1. Introduction

SWAN (Simulating WAVes Nearshore) is the third-generation surface wave model developed originally by Booij et al. (1999) and improved through a team effort (SWAN Team, 2006a). This model considers the characteristics of surface waves in shallow water by solving the wave action balance equation with inclusion of dissipation from bottom friction, triad and quadruplet wave-wave interactions, and shallow water wave-breaking (SWAN Team, 2006b). SWAN has become one of the most popular surface wave models presently available and it is widely used for coastal ocean wave simulations, engineering applications and surface wave forecasts. SWAN is discretized using a curvilinear-structured grid and solved using fully implicit finite-difference algorithms. By application of a coarse-fine grid nesting approach, SWAN can be set up with variable grids in deep and shallow ocean regions to provide high quality simulations of surface waves in the nearshore region.

Hsu et al. (2005) recently converted SWAN into a finite-element-based unstructured-grid version (hereafter referred to as FE-WAVE) for use in irregular coastal settings characterized by numerous barriers, islands, inlets and narrow navigation channels. Discretizing the wave action balance equation using a non-overlapping triangular mesh, the Taylor-Galerkin finite-element method provides an accurate geometric fitting of complex coastlines, which makes FE-WAVE more suitable for nearshore applications. Model-model comparisons of simulated waves generated by Typhoon Bilis in 2000 in the coastal region of Taiwan Strait clearly show that with better resolution of the complex coastal geometry, FE-WAVE provides a more realistic and accurate simulation of significant wave heights and dominant wave periods than is possible using the standard SWAN formulation (Hsu et al., 2005).

As an alternative unstructured-grid algorithm, the finite-volume method has recently received more attention in the coastal ocean modeling community (Casulli and Lang, 2004; Chen et al., 2003; Fringer et al., 2006). Dividing the computational domain by using a triangular mesh and solving the equations with flux-based discrete algorithms, this method takes advantage of finite-difference methods for simple code structure and computational efficiency and finite-element methods for geometric flexibility.

* Corresponding author. Address: Department of Fisheries Oceanography, School for Marine Science and Technology, University of Massachusetts-Dartmouth, 706 South Rodney French Blvd, New Bedford, MA 02744, USA. Tel.: +508 910 6388; fax: +508 910 6371.

E-mail address: c1chen@umassd.edu (C. Chen).

FVCOM (an unstructured-grid finite-volume coastal ocean model) is a state-of-the-art finite-volume coastal ocean model that has been widely used in coastal and estuarine regions (Chen et al., 2006a; Chen et al., 2006b; Chen et al., 2007). An integrated coastal ocean model system has been developed around FVCOM for the purpose of coastal environmental prediction and management (described at <http://fvcom.smast.umassd.edu/>). Implementation of an unstructured-grid surface wave model within this system makes it more suitable and reliable for application to inundation simulations (e.g., flooding due to storm surge) and studies of fishery larval recruitment problems, in which the surface waves are directly related to sediment resuspension at the ocean bottom.

By implementing finite-volume algorithms within SWAN, we have converted SWAN into an unstructured-grid finite-volume model (hereafter referred to as FVCOM-SWAVE). This model provides an alternative option for unstructured-grid wave models for the coastal ocean. FVCOM-SWAVE can also be coupled with any triangular mesh-based unstructured-grid ocean models for the study and simulation of current-wave interactions. This paper describes the finite-volume algorithms used in FVCOM-SWAVE, followed by a series of validation experiments and an example showing the application of the model to the US northeast coastal ocean.

2. Governing equation and discrete methods

2.1. Spectral action balance equation

The evolution of wave spectra is determined by the wave action density spectrum balance equation expressed as

$$\frac{\partial N}{\partial t} + \nabla \cdot [(\vec{C}_g + \vec{V})N] + \frac{\partial C_\sigma N}{\partial \sigma} + \frac{\partial C_\theta N}{\partial \theta} = \frac{S_{tot}}{\sigma} \quad (1)$$

where N is the wave action density spectrum; t is the time; σ is the relative frequency; θ is the wave direction; C_σ and C_θ are the wave propagation velocities in spectral space (σ , θ); $\vec{C}_g = \partial\sigma/\partial\vec{k}$ is the group velocity; k is the wave number vector; \vec{V} is ambient water current vector, and $\nabla \cdot (\cdot)$ is the horizontal divergence operator in geographic space. In the Cartesian coordinates, $\nabla \cdot (\cdot) = \partial(\cdot)/\partial x + \partial(\cdot)/\partial y$, while in spherical coordinates, we denote λ as longitude and φ as latitude, implying $\nabla \cdot (\cdot) = \partial(\cdot)/\partial\lambda + \cos^{-1}\varphi \partial[\cos\varphi(\cdot)]/\partial\varphi$. S_{tot} is the source-sink term given as

$$S_{tot} = S_{in} + S_{nl3} + S_{nl4} + S_{ds,w} + S_{ds,b} + S_{ds,br} \quad (2)$$

where S_{in} is the function for the wind-induced wave growth; S_{nl3} is the nonlinear transfer of wave energy due to three-wave interactions; S_{nl4} is the nonlinear transfer of wave energy due to four-wave interactions; $S_{ds,w}$ is the wave decay due to white capping; $S_{ds,b}$ is the wave decay due to bottom friction; and $S_{ds,br}$ is the wave decay due to depth-induced wave breaking. Detailed descriptions of each of these terms are given in the SWAN technical manual (SWAN Team, 2006b) and not included here.

2.2. Discretization

Following the discrete approach used in FE-WAVE (Hsu et al., 2005), we split Eq. (1) into four equations given as

$$\frac{N^{n+1/4} - N^n}{\Delta t} + \frac{\partial(C_\sigma N)}{\partial \sigma} = 0 \quad (3)$$

$$\frac{N^{n+3/4} - N^{n+1/4}}{\Delta t} + \frac{\partial(C_\theta N)}{\partial \theta} = 0 \quad (4)$$

$$\frac{N^{n+3/4} - N^{n+1/4}}{\Delta t} + \nabla \cdot [(\vec{C}_g + \vec{V})N] = 0 \quad (5)$$

$$\frac{N^{n+1} - N^{n+3/4}}{\Delta t} = \frac{S_{tot}}{\sigma} \quad (6)$$

where n denotes the n th time step, and Δt is the time interval for the numerical integration. Eqs. (3) and (4) describe the change of action density spectrum in spectral space. They are solved by the Flux Corrected Transport method (FCT) (Boris and Book, 1973; Hsu et al., 2005) and the Crank–Nicolson method (Crank and Nicolson, 1947), respectively. Eq. (5) describes the propagation of the waves in geographic space. It is solved by either an explicit finite-volume upwind advection scheme (directly adopted from FVCOM) or a semi-implicit finite-volume upwind advection scheme. Eq. (6) represents the growth, transfer and decay of the waves driven by the source terms. It is solved by a semi-implicit integration scheme as used in the WAM model (WAMDI Group, 1988) and WAVE-WATCH III model (Tolman, 2002). A brief description of the discrete algorithms used to solve Eqs. (3)–(6) is given below.

2.2.1. Action density in frequency space

The FCT method, proposed first by Boris and Book (1973), is a conservative, positive discrete algorithm suitable for steep-gradient problems without dispersively generated oscillations. The algorithm was used by Hsu et al. (2005) in FE-WAVE and also is adopted here to solve Eq. (3) in FVCOM-SWAVE. The discrete approach used in the FCT method consists of transport, anti-diffusion and correcting stages, as given by

$$N_{j\sigma}^{n+1/4} = N_{j\sigma}^n - (A_{j\sigma+1/2}^* - A_{j\sigma-1/2}^*), \quad (7)$$

where j_σ denotes the j th frequency and the resolution is specified as a “constant-relative-frequency” defined as $\Delta\sigma/\sigma$. $N_{j\sigma}^n$ represents the action density at the transport stage calculated by

$$N_{j\sigma}^* = N_{j\sigma}^n - \frac{\Delta t}{\Delta\sigma} (\Phi_{j\sigma+1/2}^1 - \Phi_{j\sigma-1/2}^1) \quad (8)$$

where Φ is the flux defined as

$$\Phi_{j\sigma+1/2}^1 = N_{j\sigma}^n \frac{C_{\sigma j\sigma+1} + |C_{\sigma j\sigma+1}|}{2} + N_{j\sigma+1}^n \frac{C_{\sigma j\sigma+1} - |C_{\sigma j\sigma+1}|}{2} \quad (9)$$

$$\Phi_{j\sigma-1/2}^1 = N_{j\sigma-1}^n \frac{C_{\sigma j\sigma} + |C_{\sigma j\sigma}|}{2} + N_{j\sigma}^n \frac{C_{\sigma j\sigma} - |C_{\sigma j\sigma}|}{2} \quad (10)$$

and the superscript “1” denotes the first stage.

$A_{j\sigma+1/2}^*$ and $A_{j\sigma-1/2}^*$ are limited anti-diffusion fluxes defined as

$$A_{j\sigma+1/2}^* = \text{sgn}(A_{j\sigma+1/2}) \max \left\{ 0, \min \left[|A_{j\sigma+1/2}|, \text{sgn}(A_{j\sigma+1/2})(N_{j\sigma+2}^* - N_{j\sigma+1}^*), \right. \right. \\ \left. \left. \times \text{sgn}(A_{j\sigma+1/2})(N_{j\sigma}^* - N_{j\sigma-1}^*) \right] \right\} \quad (11)$$

$$A_{j\sigma-1/2}^* = \text{sgn}(A_{j\sigma-1/2}) \max \left\{ 0, \min \left[|A_{j\sigma-1/2}|, \text{sgn}(A_{j\sigma-1/2})(N_{j\sigma+1}^* - N_{j\sigma}^*), \right. \right. \\ \left. \left. \times \text{sgn}(A_{j\sigma-1/2})(N_{j\sigma-1}^* - N_{j\sigma-2}^*) \right] \right\} \quad (12)$$

where

$$A_{j\sigma+1/2} = \frac{\Delta t}{\Delta\sigma} (\Phi_{j\sigma+1/2}^2 - \Phi_{j\sigma+1/2}^1); \quad A_{j\sigma-1/2} = \frac{\Delta t}{\Delta\sigma} (\Phi_{j\sigma-1/2}^2 - \Phi_{j\sigma-1/2}^1); \quad (13)$$

$$\Phi_{j\sigma+1/2}^2 = N_{j\sigma+1}^n \frac{C_{\sigma j\sigma+1} + C_{\sigma j\sigma}}{2}; \quad \Phi_{j\sigma-1/2}^2 = N_{j\sigma}^n \frac{C_{\sigma j\sigma-1} + C_{\sigma j\sigma}}{2}; \quad (14)$$

and superscript “2” denotes the second stage and $\text{sgn}(A_{j\sigma+1/2}) =$

$$\begin{cases} 1, & \text{if } A_{j\sigma+1/2} \geq 0 \\ -1, & \text{if } A_{j\sigma+1/2} < 0 \end{cases}$$

2.2.2. Action density in directional space

The action density at the $(n+2/4)$ th time step in wave directional space is calculated using a second-order accurate implicit Crank–Nicolson scheme (Crank and Nicolson, 1947) given by

$$N_{j\theta}^{n+2/4} = N_{j\theta}^{n+1/4} + \alpha \frac{\Delta t}{2\Delta\theta} \left[(C_\theta N)_{j\theta-1}^{n+2/4} - (C_\theta N)_{j\theta+1}^{n+2/4} \right] - (1-\alpha) \\ \times \frac{\Delta t}{2\Delta\theta} \left[(C_\theta N)_{j\theta+1}^{n+1/4} - (C_\theta N)_{j\theta-1}^{n+1/4} \right] \quad (15)$$

where j_0 denotes the j th direction interval and the resolution is specified by $\Delta\theta$. α is a weighting factor with a default value of 0.5.

2.2.3. Action density in geographic space

Eq. (5) is solved numerically using the unstructured-grid finite-volume approach implemented in FVCOM (Chen et al., 2003; Chen et al., 2006b) for both Cartesian and spherical coordinates. The flux form of Eq. (5) in a control volume shown in Fig. 1 can be written as

$$N^{n+3/4} = N^{n+2/4} - \frac{\Delta t}{\Omega} \sum_{i=1}^{l_n} C_{n,i} N_i \Delta l_i. \quad (16)$$

Here, Ω is the area of the control volume indicated by the dark shaded area in Fig. 1, l_i ($i = 1, l_n$) is the perimeter of Ω , l_n is the number of edges of Ω and $C_{n,i}$ is the component of $\vec{C}_g + \vec{V}$ normal to l_i . Eq. (16) is solved by either the explicit upwind scheme or semi-implicit upwind scheme. Detailed descriptions of these two solvers are given in the Appendix; the calculation of the action density at the edge of the control volume is summarized here. In the explicit approach,

$$N_i = \begin{cases} N_A^{n+2/4} + \frac{\Delta r_A}{\Omega_A} \sum_{j=1}^{l_{\Omega_A,n}} N_{\Omega_A,j}^{n+2/4} \Delta l_{\Omega_A,j} & \text{for } C_n > 0 \\ N_B^{n+2/4} + \frac{\Delta r_B}{\Omega_B} \sum_{j=1}^{l_{\Omega_B,n}} N_{\Omega_B,j}^{n+2/4} \Delta l_{\Omega_B,j} & \text{for } C_n < 0 \end{cases}, \quad (17)$$

where, respectively, N_A^n and N_B^n are the n th time step action densities at nodes of A and B; Ω_A (light dashed area in Fig. 1) and Ω_B are the total area of triangles with central nodes at A and B; $l_{\Omega_A,j}$ ($j=1, l_{\Omega_A,n}$) and $l_{\Omega_B,j}$ ($j=1, l_{\Omega_B,n}$) are the perimeters of Ω_A and Ω_B ; $l_{\Omega_A,n}$ and $l_{\Omega_B,n}$ are the number of edges of Ω_A and Ω_B ; and Δr_A and Δr_B are the distances from node A and node B to the centroids of triangles connected to nodes A and B. $C_n > 0$ refers to the outward direction of the control volume. This is the second-order approximate advection scheme used to solve the tracer equation in FVCOM.

In the semi-implicit approach, we have

$$N_i = \begin{cases} N_A^{n+3/4} + \frac{\Delta r_A}{\Omega_A} \sum_{j=1}^{l_{\Omega_A,n}} N_{\Omega_A,j}^{n+2/4} \Delta l_{\Omega_A,j} & \text{for } C_n > 0 \\ N_B^{n+3/4} + \frac{\Delta r_B}{\Omega_B} \sum_{j=1}^{l_{\Omega_B,n}} N_{\Omega_B,j}^{n+2/4} \Delta l_{\Omega_B,j} & \text{for } C_n < 0 \end{cases}. \quad (18)$$

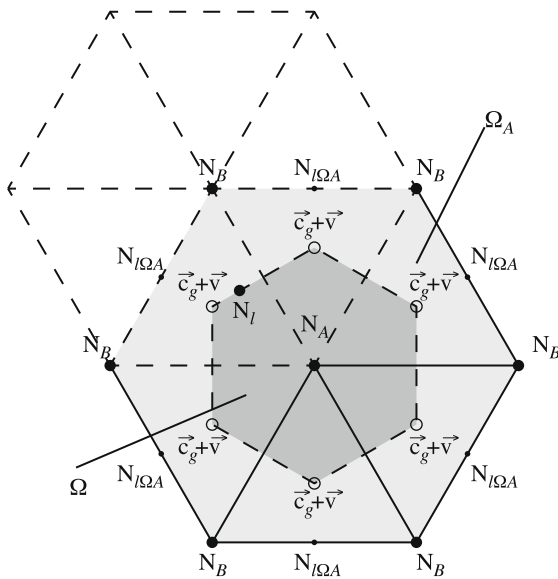


Fig. 1. Schematic of the unstructured triangular grid used for geographical spatial discretization in FVCOM-SWAVE. Definitions of variables are provided in the text.

Substituting Eq. (18) into Eq. (16) results in a 2D asymmetric and diagonally dominant matrix with a stencil equal to the sum of the surrounding node points contained in a control volume. It can be solved efficiently using a scalable sparse matrix solver library (PETSc) (Balay et al., 2007) implemented with a high performance pre-conditional HYPRE software library (HYPRE Team, 2001). This method of sparse matrix solution was implemented to solve the Poisson equation for the non-hydrostatic version of FVCOM (Lai et al., 2008).

2.2.4. Action density (N^{m+1}) related to source terms

Eq. (6) is solved using the same second-order, semi-implicit, centered-difference scheme as is implemented in WAM and WAVEWATCH-III. This is

$$N^{n+1} = N^{n+3/4} + \frac{\Delta t}{2\sigma} (S^{n+1} + S^n) \quad (19)$$

where S^{n+1} and N^{m+1} are nonlinearly coupled to each other. A detailed description of this algorithm is given by the WAMDI Group (1988) and Tolman (2002).

FVCOM-SWAVE is parallelized using the MPI framework as implemented in FVCOM, and thus can take advantage of the substantial computing power of modern multi-processor machines (Cowles, 2008). This version retains all options available for source terms in the SWAN model. The essential difference between the two models is in solving for wave propagation in geographic space by the unstructured-grid finite-volume algorithm. However, as FE-WAVE, as developed by Hsu et al. (2005), also uses the same triangular mesh approach as described in FVCOM-SWAVE, these two versions can both be run using the same grid, but with different spatial discretization (finite-volume and finite-element) methods.

3. Validation experiments

Four idealized benchmark tests were used to validate FVCOM-SWAVE with the standard SWAN model by Booij et al. (1999). These tests were designed to investigate the numerical diffusion of the discrete schemes, and to examine the properties of wave-current interactions, and wave propagation over varying shallow water topography. We also did standard growth curve analysis in idealized fetch-limited cases, following the SWAMP Group (1985), with a constant wind blowing seaward off a long straight coastline (as shown in Booij et al. (1999)). The same procedures are used to compare FVCOM-SWAVE and SWAN in all four idealized tests. Comparisons are made directly with the standard SWAN model, which has been previously very carefully compared and calibrated to growth curve data (by Booij et al. (1999)).

Inter-model or model-data comparisons in this text were made based on both RMS and RMS (%). For the significant wave height, H_s , the RMS (%) is defined as

$$RMS = \sqrt{\frac{1}{N-1} \sum_{i=1}^N [H_{s,m}(i) - H_{s,o}(i)]^2} \quad (20)$$

$$RMS(\%) = \sqrt{\frac{1}{N-1} \sum_{i=1}^N \left[\frac{H_{s,m}(i) - H_{s,m}|_{\min}}{H_{s,m}|_{\max} - H_{s,m}|_{\min}} - \frac{H_{s,o}(i) - H_{s,o}|_{\min}}{H_{s,o}|_{\max} - H_{s,o}|_{\min}} \right]^2}. \quad (21)$$

In the model-data comparison cases, $H_{s,m}$ and $H_{s,o}$ are the model-predicted and observed H_s , respectively. Here, N is the sample number, and the subscripts “max” and “min” indicate maximum and minimum. For the dominant wave period, RMS (%) is calculated by replacing H_s by T_p (dominant peak wave periods) in expression (21). In these inter-model comparison cases, the subscript “m” represents FVCOM-SWAVE and “o” represents SWAN.

3.1. Numerical diffusion

Consider a harmonic, long-crested wave propagating through a gap into a square computational domain with dimensions 10×10 km in deep water (Fig. 2). The open gap is located in the lower left corner of the domain, so that the wave propagates along the diagonal at an angle of 45° with respect to the positive x -axis (x is the east–west coordinate which is positive in the eastward direction). This harmonic wave is simulated using a Gaussian-shaped frequency spectrum with a peak frequency of 0.1 Hz, a standard deviation of 0.01 Hz and a resolution defined as 3% of the relative frequency. The significant wave height at the gap is 1.0 m, and the long crest of the wave is calculated using an assumed $\cos^{500}(\theta)$ directional distribution.

The computational domain is tessellated with a square grid for SWAN and with right triangles for FVCOM-SWAVE. The right triangles are constructed by dividing each square along its diagonal line. The horizontal resolution for SWAN is 100 m, which is the same for FVCOM-SWAVE, where the horizontal resolution is defined using the shortest edge of a computational cell. The resolution in directional space is 0.5° . Here, the time step in SWAN and FVCOM-SWAVE is specified to maintain stability.

For this case, SWAN was run using three different discrete schemes: (a) the first-order, backward space and backward time scheme for stationary waves (BSBT), (b) the second-order upwind iteration scheme for stationary waves (SORDUP) (Rogers et al., 2002), and (c) the third-order *Stelling–Lendretse* scheme. FVCOM-SWAVE was run using both explicit and implicit second-order finite-volume upwind schemes.

The SWAN and FVCOM-SWAVE significant wave height distributions are compared in Fig. 2. The width of the spreading of the significant wave height field is used as an index for numerical diffusion. In general, the SORDUP result has the least numerical diffusion, whereas BSBT gives the largest numerical diffusion.

Respectively, at distances of 1 and 5 km in the x - and y - axes away from the source, the width of the wave height field is 1.75 and 2.5 km for the first order BSBT, 1.0 and 1.5 km for the second order SORDUP, 1.5 and 1.75 km for the third-order *Stelling–Lendretse* scheme, and 0.75 and 1.75 km for FVCOM-SWAVE. At these two locations, FE-WAVE gives the same widths as FVCOM-SWAVE. If only the non-stationary numerical schemes are considered, we find that the second-order finite-volume upwind scheme used in FVCOM-SWAVE can reach the same level of numerical accuracy as the third-order *Stelling–Lendretse* scheme, and can exceed this level of accuracy in the region close to the gap. In this special case, the effective horizontal resolution is the same for both SWAN and FVCOM-SWAVE, because the computational cells have equivalent area. Because BSBT is a first-order approximation, it is not surprising that this scheme (used in SWAN) generates the largest numerical diffusion. In the most current version of SWAN, this scheme is only used in cells connected to solid boundaries for both stationary and non-stationary waves.

In executing this comparison experiment, we have followed the approaches used in Booij et al. (1999) and Hsu et al. (2005). It should be noted that this benchmark test case only provides the relative numerical diffusion between these different finite-difference and finite-volume schemes, because the accuracy of the wave field can be affected significantly by the finite-resolution discretization that is used in frequency and directional space. A more objective comparison should be made based on the so-called garden sprinkler problem (SWAMP Group, 1985). This problem was not examined in our current SWAN and FVCOM-SWAVE comparison experiments.

3.2. Wave-current interactions

This idealized case considers propagation of waves in a deepwater region in the presence of a uniform background current. Four

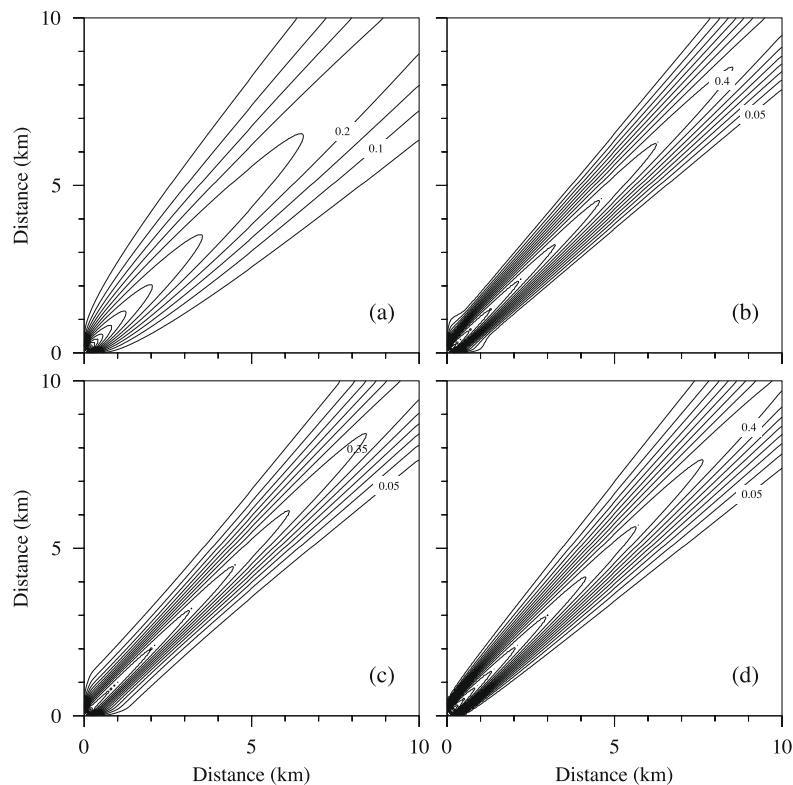


Fig. 2. Spatial distributions of the significant wave height (m) for a harmonic wave propagating along a diagonal line in a square computational domain. (a) SWAN-BSBT; (b) SWAN-SORDUP; (c) SWAN-SL; and (d) FVCOM-SWAVE.

cases are tested: (a) wave propagation opposite to the direction of the current; (b) wave propagation in the same direction as the current; (c) wave propagation against the current at an angle of 30°; and (d) wave propagation in the direction of the current at an angle of 30°. These four cases are shown schematically in Fig. 3.

The computational domain consists of a rectangle of length 4 km and width 10 km. The assumed waves have the same distribution and shape as those in the previous test case (3.1) and they are specified along the left boundary with a direction of propagation as shown in Fig. 3. In cases (a) and (b), the speed of the current increases in the down-wave direction, ranging from 0.0 to 2.0 m/s. In cases (c) and (d), the current is rotated by 90°. The SWAN implementation employed a rectangular grid with a horizontal resolution of 40 m in the direction of the wave propagation (x -axis) and 100 m in the cross-wave direction (y -axis). To maintain the same spatial resolution as SWAN in the direction of wave propagation, a mesh of equilateral triangles with an edge length of 40 m was used for FVCOM-SWAVE. SWAN was run using the third-order Stelling–Leendertse scheme and FVCOM-SWAVE was run using the second-order semi-implicit upwind scheme.

Given the same resolution in the wave propagation direction, the distributions of significant wave height and mean wave direction in the x -direction calculated by SWAN and FVCOM-SWAVE are almost identical (Fig. 4) and match well with the analytical solution. The root-mean-square (RMS) differences of significant wave height (H_s) and direction (θ) between SWAN and FVCOM-SWAVE for the four cases in this experiment are calculated. The correlation coefficients of these two models for H_s and θ are essentially 1.0, and the RMS (%) difference (see the definition given in Eq. (21)) is ~ 0.44 (or less) for H_s and ~ 0.004 (or less) for θ . This demonstrates that the second-order finite-volume advection scheme used in FVCOM-SWAVE has an equivalent accuracy as the third-order finite-difference scheme used in SWAN. For this idealized domain, the fact that the wave features from structured-grid SWAN runs can be exactly reproduced using an unstructured-grid finite-volume model suggests that the finite-volume flux algorithm used in FVCOM-SWAVE can ensure high numerical accuracy with little influence from the irregular grid. This suggests that the geometric grid flexibility of FVCOM-SWAVE makes it a good candidate to simulate wave-current interactions in complex coastal regions with strong currents, headlands, islands, and irregular channels.

Hsu et al. (2005) used FE-WAVE model to conduct the same experiment. The agreement of their solution with the original SWAN varies with the x -axis. The match is good over a distance

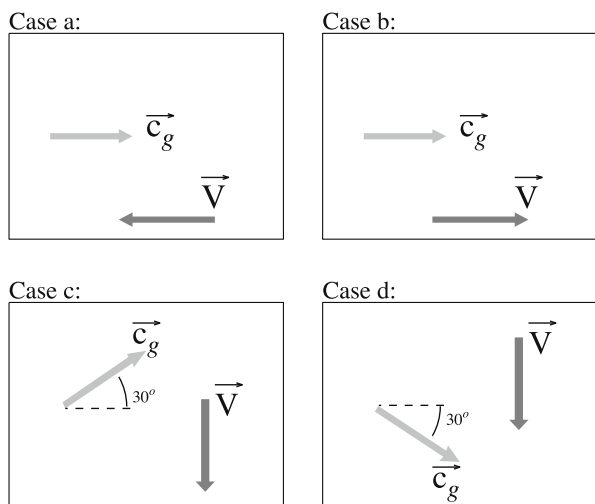


Fig. 3. Schematic of the surface wave propagation in a domain with an ambient water current. \vec{c}_g is the wave group velocity and \vec{V} is the water current vector.

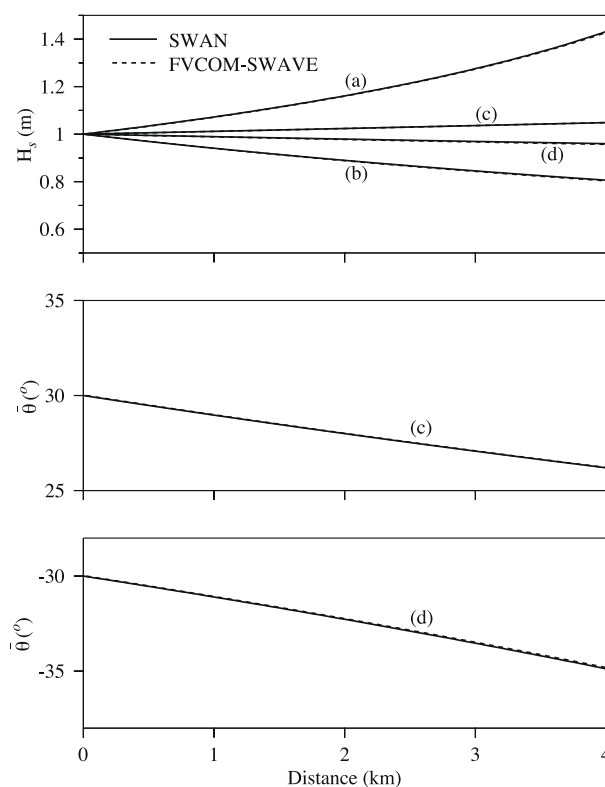


Fig. 4. Cross-isobath distributions of the SWAN and FVCOM-SWAVE predicted significant wave heights and wave propagation directions for cases (a), (b), (c), and (d) shown in Fig. 3. Solid line: SWAN, and dashed line: FVCOM-SWAVE.

of less than 3.0 km, but a significant bias occurs over the remainder of the domain. In this test case, the unstructured-grid finite-volume algorithm used in FVCOM-SWAVE seems to show more promise than the unstructured-grid finite-element method used by Hsu et al. (2005). However, as the FE-WAVE model is not an open source code, the comparison made here is only based on Figs. 2 and 3 in Hsu et al. (2005).

3.3. Wave shoaling and refraction

Consider surface waves propagating towards a straight beach. The water depth varies from the deeper outer region with a depth of 20 m, to zero at the coast over a distance of 4.0 km. Two cases are examined: (a) incident waves propagating in the direction perpendicular to the coastline and (b) incident waves propagating towards to the coast with an angle of 30° (Fig. 5). These two cases are designed to examine wave shoaling and refraction without wave-current interaction.

The wave model boundary conditions and set-up at the deep open boundary are the same as those given in Section 3.2. The horizontal computational domain consists of a rectangular area with a width of 20 km (y -axis) and a length of 4 km (x -axis). For SWAN, we use a rectangular grid with a resolution of 40 m in the x -axis (cross-isobath direction) and 200 m in the y -axis (along-isobath direction). To have the same resolution in the cross-isobath direction, FVCOM-SWAVE uses an equilateral triangular grid with a length of 40 m.

Running SWAN with the third-order Stelling–Leendertse scheme produces exactly the same results as those shown in Booij et al. (1999). The model solution matches the analytical solution from linear wave theory, with an error of 0.1% in significant wave height and of $< 0.25^\circ$ in direction within the region with water depth > 0.05 m. Given the same horizontal resolution, FVCOM-SWAVE predicts a nearly identical solution to that of SWAN for both the

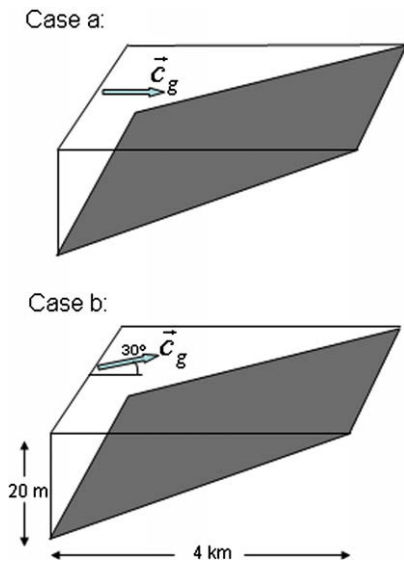


Fig. 5. Schematic of the surface wave propagating towards the coast from the deepwater region to the shallow shelf. Case (a): shoaling experiment; case (b): refraction experiment.

shoaling and refraction cases (Fig. 6). Considering the same domain with water depth >0.05 m, the correlation coefficient of these two model results is essentially 1.0 for all cases, and the RMS(%) difference is 1.84 (or less) for H_s and 0.63 (or less) for θ . However, FE-WAVE shows a relatively larger bias in comparison with SWAN (Figs. 4 and 5 in Hsu et al. (2005)), and in fact the bias suggested for FE-WAVE appears to be larger than that for FVCOM-SWAVE.

3.4. Growth curves for wind-generated waves

In studying growth curves for these two model systems, we used the same source term formulations for FVCOM-SWAVE as we used for SWAN (the so-called WAM cycle 3 physics). We assumed a constant wind of 20 m/s at 10-m reference height off a long, straight coastline in a rectangular domain with dimensions

Table 1

Parameters used in SWAN and FVCOM-SWAVE setups

Parameters	Definition	Value
cds2	Coefficient used to determine the rate of whitecapping dissipation	2.36×10^{-5}
stpm	Value of the wave steepness for the Pierson–Moskowitz	3.02×10^{-5}
a	Proportionality coefficient in the case with inclusion of Cavaleri and Malanotte's wave growth term	0.0015
alpha	Proportionality coefficient of the rate of dissipation	1.0
gamma	The ratio of maximum individual wave height over depth	0.73
cfjon	Coefficient of the JONSWAP formulation	0.067
iquad	Fully explicit computation of the nonlinear transfer with DIA per iteration	2
lambda	Coefficient for quadruplet configuration in the case of DIA	0.25
Cnl4	Proportionality coefficient for quadruplet interactions in case of DIA	3×10^7
Csh1	Coefficient for shallow water scaling in case of DIA	5.5
Csh2	Coefficient for shallow water scaling in case of DIA	6/7
Csh3	Coefficient for shallow water scaling in case of DIA	1.25

consisting of a length of 400 km in the along-coast direction (y-axis) and a width of 9000 km in the cross-coast direction (x-axis). The ocean is assumed to be infinitely deep. We compared the growth curves of total wave energy and peak frequency as estimated by FVCOM-SWAVE and SWAN. Both FVCOM-SWAVE and SWAN are run with a cross-coastal resolution of 10 km. The parameters used in the model setups are based on the values listed in

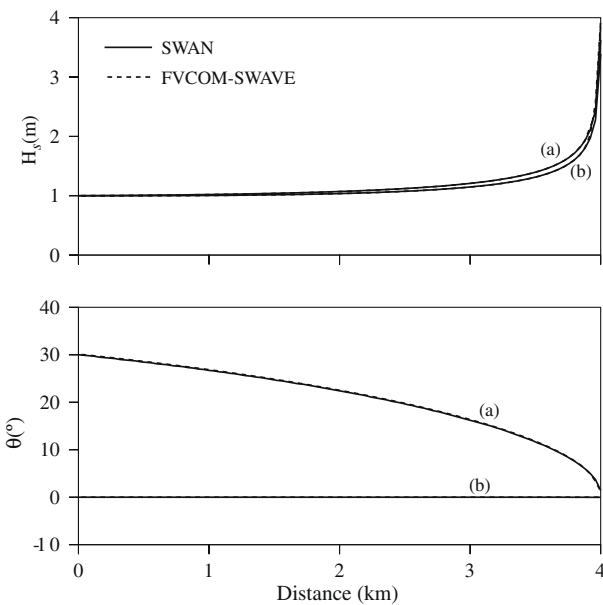


Fig. 6. Cross-isobath distributions of the SWAN and FVCOM-SWAVE predicted significant wave height and wave propagation directions for cases (a) and (b) shown in Fig. 5. Solid line: SWAN, and dashed line: FVCOM-SWAVE.

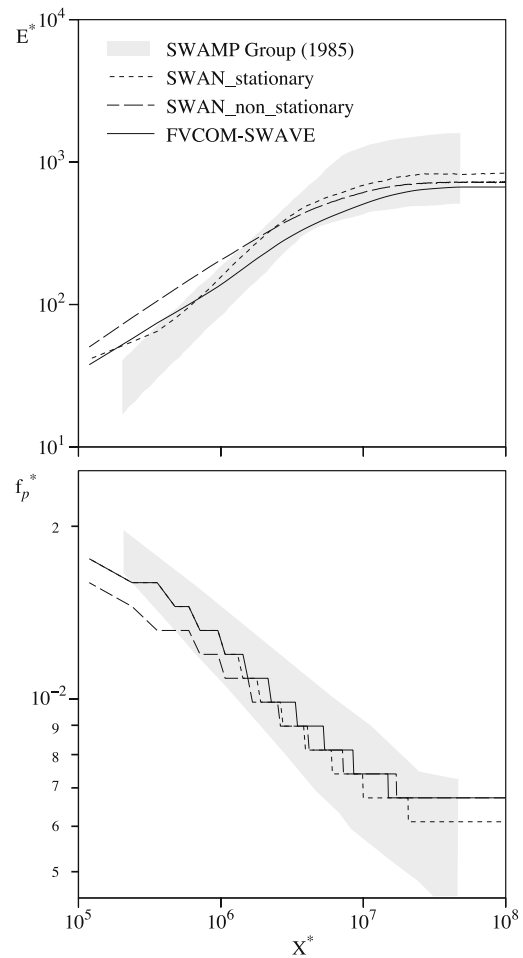


Fig. 7. Distributions of dimensionless fetch-limited growth curves for the total wave energy E^* (a) and peak frequency f_p^* as a function of dimensionless fetch for FVCOM-SWAVE, stationary and non-stationary SWAN.

Table 1, as documented by the SWAN Team (2006a,b), with the WAM cycle 3 physics.

In this case, FVCOM-SWAVE and SWAN show similar growth curves in dimensionless wave energy ($E^* = g^2 E / U_*^4$) and dimensionless peak frequency ($f_p^* = U_* f_p / g$) as functions of dimensionless fetch ($X^* = gX / U_*^2$) (Fig. 7). Here E is the total wave energy, g is the gravitational acceleration, U^* is the friction velocity at the sea surface, namely $U_*^2 = C_D U_{10}^2$ (where C_D is the drag coefficient following Wu (1982), U_{10} is the wind speed at the 10-m height above the sea surface) and X is the fetch.

For large fetch, $X^* > 10^6$, the dimensionless total energies of FVCOM-SWAVE and SWAN (stationary and non-stationary cases) are within the variations shown by models considered by the SWAMP Group (1985). For smaller fetch, $X^* < 10^6$, the growth curve for FVCOM-SWAVE is very close to that shown for the stationary SWAN run; however these curves are significantly lower than that resulting from the non-stationary SWAN run. Similarly, both FVCOM-SWAVE and non-stationary SWAN-predicted peak frequencies are within the range of variation examined by the SWAMP Group (1985), except for very small fetches of $X^* \sim 10^5$. In this case, the SWAN results are identical to those shown by Booij et al. (1999). The results of this comparison are consistent with the findings of Hsu et al. (2005). The latter pointed out that in its non-stationary mode, SWAN significantly overestimates the total wave energy growth curve as a function of fetch where $X^* < 10^6$. Here, we show that this bias is resolved by the non-stationary mode of FVCOM-SWAVE.

4. Application to the Gulf of Maine

4.1. Design of numerical experiments

The Gulf of Maine (GoM) is located along the US northeast coast. It is a semi-enclosed basin opening to the North Atlantic Ocean

(NA) (Fig. 8). The GoM bathymetry features several deep basins, submarine banks, and shallow shelves connected to coastal inlets, bays and estuaries. One of the primary objectives of developing FVCOM-SWAVE is to include it in the FVCOM-based unstructured-grid Northeast Coastal Ocean Forecast System (NECOFS) (see <http://fvcom.smast.umassd.edu/>). Thus, the coupled model system would be able to make predictions of wind-induced surface waves and their coupling with other physical processes (e.g., wave setup, wave-current interaction, sediment transport) in this region, with its complex inner shelf bathymetry and irregular coastline. To validate the accuracy and reliability of FVCOM-SWAVE for this region, we used this model to simulate January 2007.

In fact, the GoM FVCOM-SWAVE grid covers the entire US east coast region with an open boundary running from a land point at about 65°W, 10°N towards the northeast to about 20°W, 50°N and then turning towards the east coast of Greenland (Fig. 9). The computational domain consists of the unstructured triangular grid, with a horizontal resolution varying from ~25 to 50 km in the interior of the NA to 0.5–1.0 km along the coast of the GoM, New England Shelf, Long Island Sound and over Georges Bank (Fig. 10). The total number of nodes is 30760 and total number of cells is 57013. Although our main interest is in the GoM and adjacent coastal regions, running FVCOM-SWAVE in this large domain can minimize open boundary issues. The flexibility in the spatial discretization enabled through the use of unstructured meshes allows coarse resolution in the open ocean and fine resolution in the coastal region, with limited reduction in computational efficiency. In January 2007, westerly wind prevailed over the GoM region. The dominant wind patterns blew from the land to the ocean, so that essentially no wave forcing was required to specify the remote open boundary. In this application experiment, no ambient currents were included.

The GoM FVCOM-SWAVE was driven by the wind fields derived from the GoM-WRF (Weather Research and Forecast) and the NA-WRF models. The GoM-WRF model was established as a part of NE-

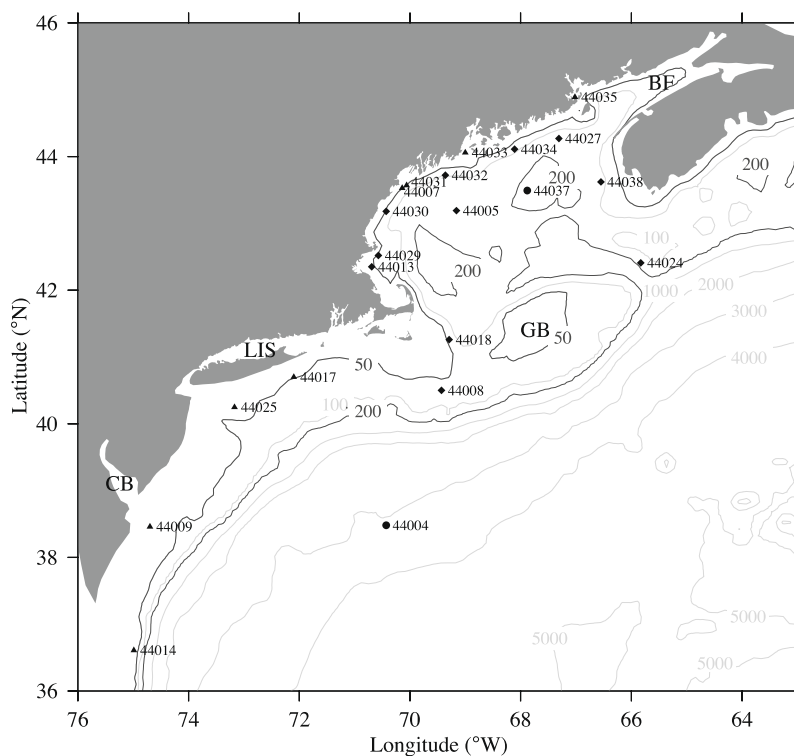


Fig. 8. Locations of NDBC environmental buoys in the US northeast coastal region used for the model-data comparison. GoM, Gulf of Maine; BF, Bay of Fundy; GB, Georges Bank; LIS, Long Island Sound; CB, Chesapeake Bay. Filled triangles: buoys located in zone 1 (water depths <50 m); filled diamonds: buoys located in zone 2 (water depths in 50–200 m range); and filled circles: buoys located in zone 3 (water depths >200 m). The number listed on each buoy is its name.

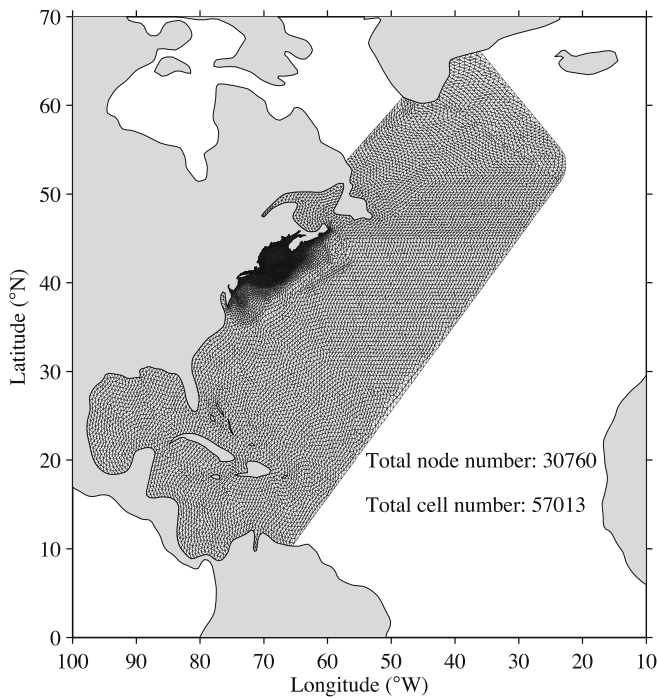


Table 2

Correlations and RMS (%) errors of assimilated wind speed via observations at buoy stations.

Buoy station identification	Sample number	Correlation coefficient	RMS error (%)
44004	734	0.84	1.25
44005	742	0.95	1.11
44007	743	0.87	1.48
44009	744	0.87	1.29
44013	739	0.92	0.99
44014	741	0.84	1.46
44017	743	0.87	1.29
44018	698	0.94	0.83
44024	692	0.92	0.98
44025	741	0.87	1.32
44027	743	0.94	0.85
44029	740	0.88	1.38
44030	740	0.90	1.17
44031	698	0.87	1.45
44032	728	0.90	1.14
44033	724	0.85	1.71
44034	704	0.92	1.07
44035	600	0.74	2.73
44037	668	0.94	0.82
44038	728	0.93	0.89
Mean		0.89	1.26

Fig. 9. Unstructured grid of the FVCOM-SWAVE configured for the US northeast coastal region.

COFS and uses a 9-km horizontal resolution covering the entire GoM and adjacent New England Shelf and Scotian Shelf. Hourly wind velocity data from all meteorological buoys in these regions were assimilated into this weather model to produce a reliable and accurate wind field. Since most buoys were located near the western NA coast, the assimilation helped reduce the RMS errors of the WRF winds in this region (Table 2). In the region outside of the GoM-WRF domain, we used the reanalysis 3-hourly 32-km resolution NA-WRF-predicted wind fields (available at <http://nomads.ncdc.noaa.gov/>). Linear interpolation was used to merge NA-WRF and GoM-WRF outputs to form an hourly wind-forcing field covering the entire computational domain. Although this approach tends to “filter” out wind variations with time scales < 3 h

in the NA-WRF region, it causes little influence on the wave simulation in the GoM and adjacent coastal regions where only the hourly GoM-WRF winds were used.

The source terms used in GoM FVCOM-SWAVE were the same as those used in the SWAN simulations. The wave growth due to wind input (S_{in}) is determined by the sum of linear and exponential growths. The linear term is specified by an empirical formula of Cavalieri and Malanotte-Rizzoli (1981) with a filter for the truncation at the Pierson–Moskowitz frequency (Pierson and Moskowitz, 1964). The exponential wave growth term is specified using Komen et al. (1984)’s empirical expression that is a function of inverse wave age U^*/c_{ph} (where c_{ph} is the phase speed). The dissipation includes white-capping, $S_{ds,w}$, bottom friction, $S_{ds,b}$, and depth-induced breaking, $S_{ds,br}$. $S_{ds,w}$ is derived from Hasselmann (1974)’s pulse-based model, $S_{ds,b}$ follows from the “JONSWAP” empirical function with Collins (1972)’s drag law expression and Madsen et al. (1988)’s eddy-viscosity formulation. $S_{ds,br}$ is

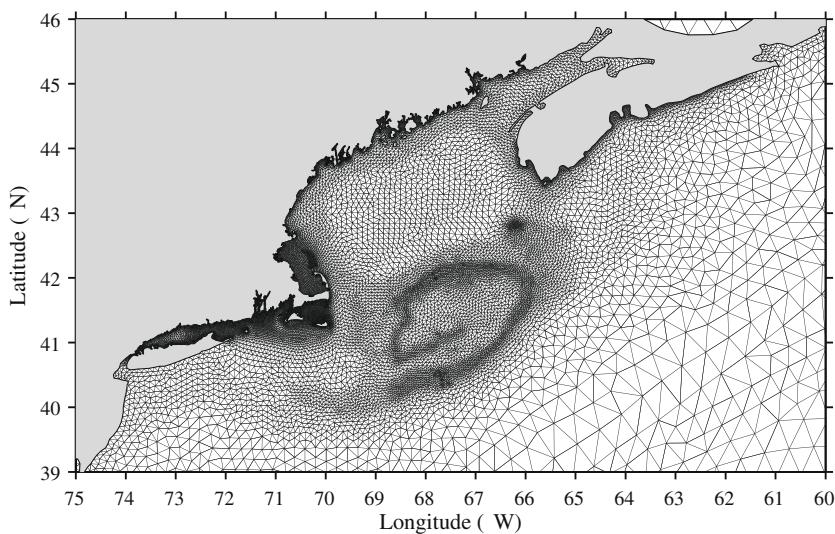


Fig. 10. An enlarged view of the unstructured triangular grid in the Gulf of Maine and New England Shelf region. The horizontal resolution of the grid varies from 25 km off Georges Bank to 0.5–1.0 km near the coast.

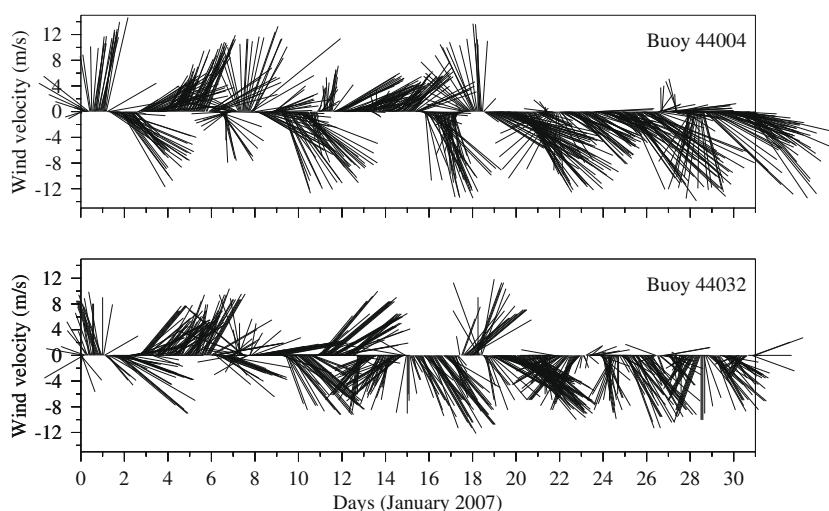


Fig. 11. Time series of wind velocity at the 10-m height above the sea surface at buoy 44004 and buoy 44032 for January 1–31, 2007.

estimated by the bore-based function derived by Battjes and Janssen (1978). The nonlinear transfer of wave energy due to wave-wave interactions is calculated by a sum of S_{nl3} (triad wave interactions) and S_{nl4} (quadruplet wave interactions). S_{nl3} is estimated from the Lumped Triad Approximation (LTA) derived by Eldeberky (1996) and S_{nl4} is specified by the Discrete Interaction Approximation (DIA) by Hasselmann et al. (1985). The parameters used in this experiment are shown in Table 1; detailed definitions are given by the SWAN Team (2006b).

The GoM FVCOM-SWAVE results are compared with significant wave height and period data recorded by 21 NOAA buoys. The buoy locations are shown in Fig. 8 and the data are available at the National Data Buoy Center (<http://www.ndbc.noaa.gov/hmd.shtml>). To evaluate the performance of GoM FVCOM-SWAVE as a function

of water depth, we divided the computational domain into three zones. Letting h be the mean water depth, zone 1 refers to the region in which $h < 50$ m; zone 2 is the region with $50 \text{ m} \leq h \leq 200$ m, and zone 3 is the region with $h > 200$ m. There are 8 buoys in zone 1, 11 buoys in zone 2 and 2 buoys in zone 3.

4.2. Model-data comparisons

During January 2007, the GoM surface weather was characterized by cold-air frontal passages with a typical time scale of 3–5 days before January 20; thereafter, the area was dominated by southeastward to southward winds that were comparatively more steady (Fig. 11). The maximum 10-m wind speed was ~ 10 –13 m/s.

Table 3

Mean and standard deviations (SD) of observed and calculated significant wave heights, correlation coefficients, and RMS errors at buoy stations.

Station (sample number)	Mean \pm SD (observed) (m)	Mean \pm SD (calculated) (m)	Correlation coefficient	RMS (m)	RMS (%)
Zone 1 ($h < 50$ m)					
44033 (701)	0.73 \pm 0.36	1.15 \pm 0.34	0.60	0.53	24.9
44031 (693)	1.06 \pm 0.52	0.93 \pm 0.37	0.75	0.37	21.2
44007 (733)	0.95 \pm 0.50	0.87 \pm 0.35	0.73	0.35	22.4
44017 (733)	1.51 \pm 0.64	1.41 \pm 0.50	0.84	0.36	17.6
44025 (726)	1.42 \pm 0.62	1.39 \pm 0.49	0.83	0.35	16.4
44009 (739)	1.30 \pm 0.52	1.30 \pm 0.42	0.75	0.35	17.0
44014 (741)	1.62 \pm 0.74	1.53 \pm 0.47	0.86	0.41	11.9
Mean	1.23 \pm 0.56	1.23 \pm 0.42	0.77	0.39	18.8
Zone 2 ($50 \text{ m} \leq h \leq 200 \text{ m}$)					
44027 (742)	1.77 \pm 0.92	1.62 \pm 0.69	0.83	0.54	13.0
44034 (677)	1.62 \pm 0.85	1.46 \pm 0.62	0.83	0.51	20.6
44032 (726)	1.40 \pm 0.68	1.27 \pm 0.49	0.71	0.50	24.3
44030 (736)	0.99 \pm 0.44	0.98 \pm 0.36	0.67	0.33	20.3
44029 (734)	0.99 \pm 0.44	0.95 \pm 0.36	0.64	0.35	36.4
44013 (737)	0.93 \pm 0.46	0.88 \pm 0.40	0.72	0.33	20.5
44018 (558)	1.78 \pm 0.70	1.85 \pm 0.67	0.86	0.36	15.3
44008 (729)	2.33 \pm 0.90	1.99 \pm 0.74	0.87	0.57	13.2
44038 (719)	2.18 \pm 1.06	1.99 \pm 0.88	0.86	0.57	11.2
44005 (479)	1.81 \pm 0.80	1.52 \pm 0.60	0.83	0.50	12.8
44024 (700)	2.71 \pm 1.30	2.21 \pm 0.87	0.86	0.88	13.0
Mean	1.68 \pm 0.78	1.16 \pm 0.61	0.79	0.49	18.2
Zone 3 ($h > 200 \text{ m}$)					
44037 (690)	2.03 \pm 0.97	1.88 \pm 0.80	0.83	0.56	12.7
44004 (734)	2.70 \pm 1.26	2.23 \pm 0.89	0.91	0.76	17.4
Mean	2.37 \pm 1.11	2.06 \pm 0.85	0.87	0.66	15.1

Table 4

Mean and standard deviations (SD) of observed and calculated peak wave periods, correlation coefficients, and RMS errors at buoy stations.

Station (Sample number)	Mean \pm SD (observed) (sec)	Mean \pm SD (calculated) (sec)	Correlation coefficient	RMS (sec)	RMS (%)
Zone 1 ($h < 50$ m)					
44033 (659)	5.84 \pm 2.71	6.27 \pm 2.28	0.22	3.17	33.0
44031 (679)	6.30 \pm 2.65	6.82 \pm 2.38	0.27	3.09	32.0
44007 (733)	7.36 \pm 3.12	7.10 \pm 2.23	0.41	3.00	26.7
44017 (733)	6.64 \pm 1.93	6.87 \pm 1.64	0.28	2.17	27.8
44025 (726)	6.36 \pm 1.96	6.50 \pm 1.76	0.38	2.08	23.4
44009 (739)	6.01 \pm 2.13	6.51 \pm 2.26	0.34	2.58	23.4
44014 (741)	7.27 \pm 1.87	7.05 \pm 2.03	0.17	2.52	23.5
Mean	6.54 \pm 2.34	6.73 \pm 2.08	0.30	2.66	27.1
Zone 2 ($50 \text{ m} \leq h \leq 200 \text{ m}$)					
44027 (742)	6.85 \pm 2.15	6.78 \pm 2.02	0.49	2.10	23.2
44034 (677)	6.92 \pm 2.62	7.09 \pm 2.02	0.34	2.71	24.9
44032 (723)	6.59 \pm 2.60	6.55 \pm 2.30	0.39	2.72	30.4
44030 (735)	6.13 \pm 2.79	6.90 \pm 2.78	0.25	3.50	33.6
44029 (734)	5.54 \pm 2.42	5.97 \pm 2.79	0.41	2.89	28.6
44013 (737)	5.31 \pm 2.88	6.10 \pm 3.04	0.46	3.18	32.5
44018 (558)	7.32 \pm 1.69	7.19 \pm 1.56	0.38	1.83	21.1
44008 (729)	7.54 \pm 1.64	7.21 \pm 1.48	0.40	1.75	20.5
44038 (719)	7.24 \pm 2.00	7.09 \pm 1.55	0.44	1.92	24.9
44005 (479)	6.51 \pm 1.98	6.89 \pm 2.19	0.46	2.42	25.6
44024 (700)	8.09 \pm 2.06	7.75 \pm 1.78	0.44	2.09	29.6
Mean	6.73 \pm 2.26	6.86 \pm 2.14	0.41	2.46	26.8
Zone 3 ($h > 200 \text{ m}$)					
44037 (690)	6.80 \pm 1.91	6.73 \pm 1.57	0.43	1.88	23.7
44004 (734)	7.81 \pm 1.65	7.35 \pm 1.61	0.58	1.57	15.3
Mean	7.30 \pm 1.78	7.04 \pm 1.59	0.51	1.73	19.5

As shown in Fig. 11, the wind speed and direction varied significantly from the near-coastal regions to the open ocean, which is

evident at buoy 44032 (~50-m isobath) and buoy 44004 (~3182-m isobath).

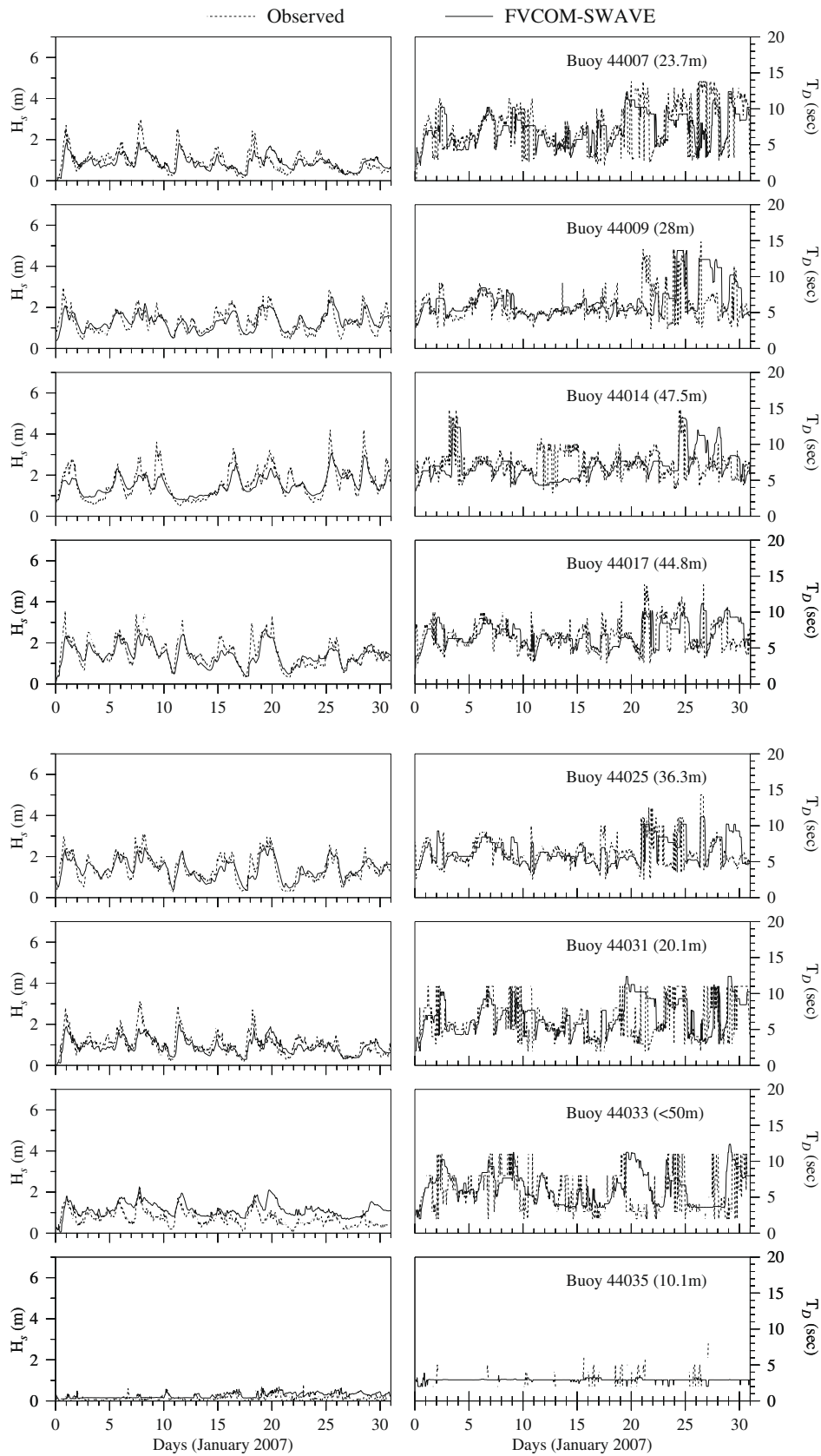


Fig. 12. Comparisons of the GoM FVCOM-SWAVE predicted (solid line) and observed (dashed line) significant wave heights (left) and dominant wave periods (right) at buoys in zone 1 (water depth <50 m).

The GoM FVCOM-SWAVE simulation performed reasonably well in capturing the spatial and temporal variability of wind-induced surface waves along the coast. Tables 3 and 4 show the means, standard deviations (SD), correlation coefficients, RMS and RMS (%) errors of H_s and T_p at buoy locations. The mean and SD values are calculated based on the measured data used in this comparison. In zone 1 (in water depth <50 m), the observations show that the peak H_s values are ~1–3 m in the near-coastal regions with mean values of 0.7–1.6 m and standard deviations of 0.4–0.7 m. We neglect buoy 44035 in this comparison because it was located in a sheltered area (in Passamaquoddy Bay) not open to wind-generated waves of the GoM and had high errors in the wind fields and recorded very low values for H_s ~0.1–0.3 m. These spatial and temporal distributions were well captured by the GoM FVCOM-SWAVE (Fig. 12). The model-predicted H_s estimates were in good agreement with 7 near-shore coastal buoys ranging from the Bay of Fundy to the Chesapeake Bay. The model predicted means and standard deviations of H_s show the same range as observations: the RMS (%) error varying from 11.9 to 24.9 with a mean RMS (%) error of 18.8. The largest observed H_s values occurred in zone 2, in the range of 1–7 m with maximum mean and standard deviation values of 2.7 and 1.3 m. The GoM FVCOM-

SWAVE reasonably captured the temporal variation in wave heights that were observed (Fig. 13). C_r was 0.64–0.87, with RMS (%) error varying from 11.2 to 36.4 with a mean RMS (%) error of 18.2. In zone 3, the peaks of the observed H_s values are similar to those found in zone 2. The GoM FVCOM-SWAVE reliably simulated the H_s peaks (Fig. 14), with C_r in the range of 0.83–0.91, RMS(%) errors of 12.7 and 17.4 and a mean RMS(%) error of 15.1.

The model-predicted T_p values have a low correlation with observations in all three zones, although the model clearly captures the wind-induced temporal variation pattern for T_p . The model-predicted means and standard deviations of T_p are in agreement with the range of the observations. The mean RMS (%) error for zone 1 is 27.1, which is comparable with our value of 26.8 for zone 2. A close examination of the differences in the model and observed T_p time series in Figs. 12–14 shows that the observations exhibit more notable variation with time than the model. In particular, the GoM FVCOM-SWAVE estimates show a tendency to under-predict observed T_p peaks. Although this can be attributed to biases in the wind fields and model inadequacies, it results from the common tendency of spectra to have multiple peaks and thus T_p estimates vary among the competing spectral peaks.

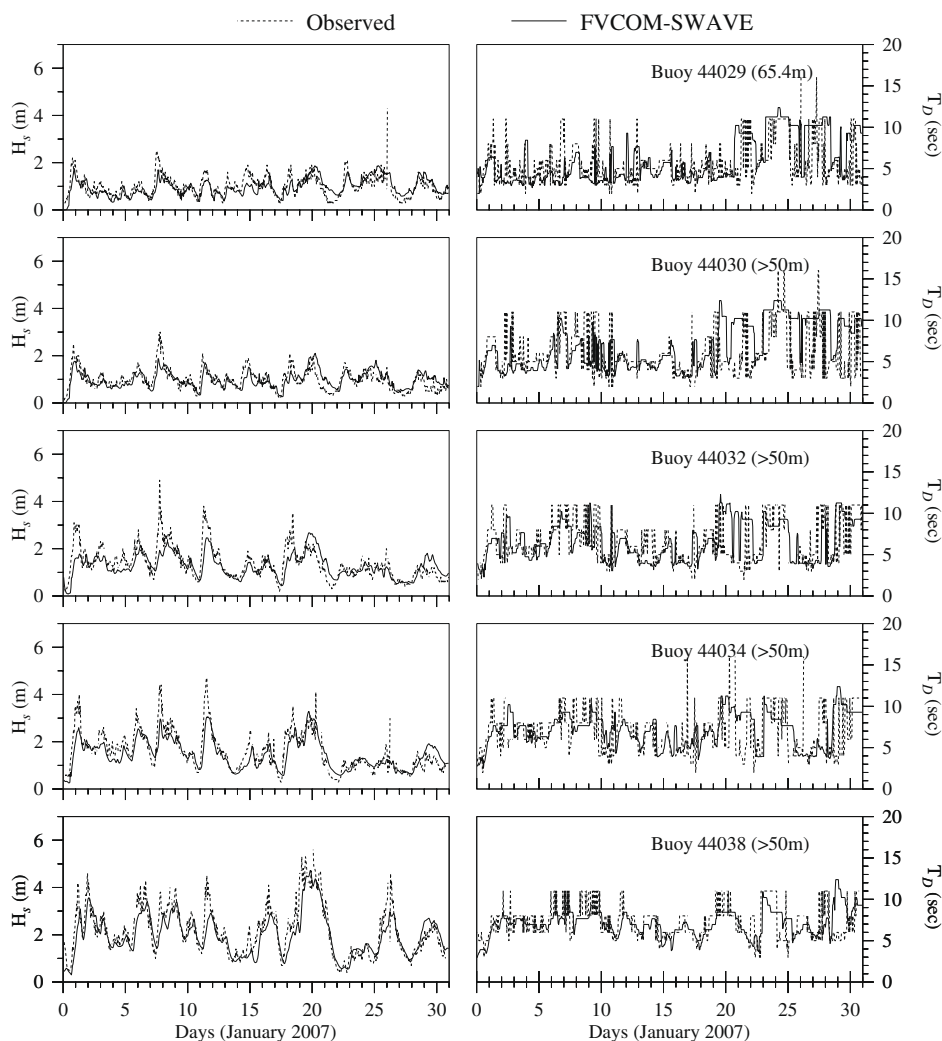


Fig. 13. Comparisons of the GoM FVCOM-SWAVE predicted (solid line) and observed (dashed line) significant wave heights (left) and dominant wave periods (right) at buoys in zone 2 (water depth in the range 50–200 m).

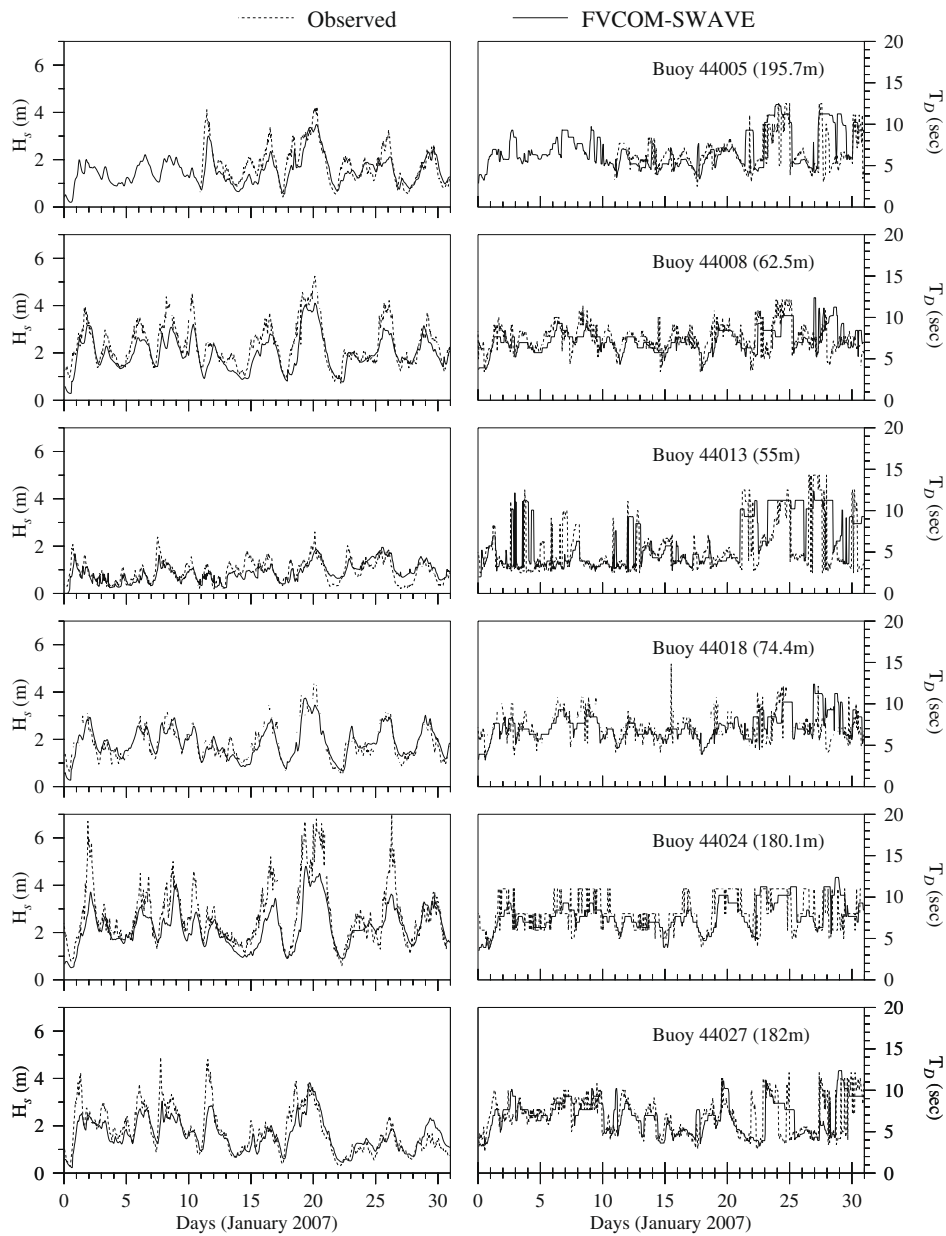


Fig. 13 (continued)

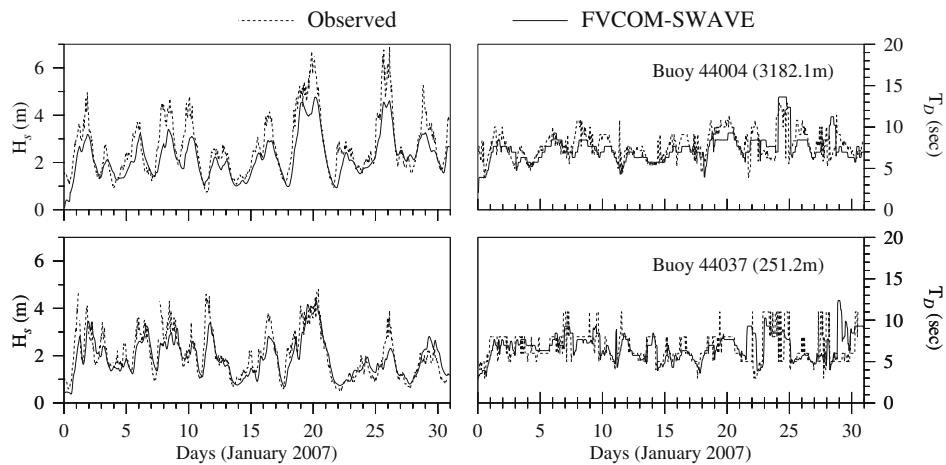


Fig. 14. Comparisons of the GoM FVCOM-SWAVE predicted (solid line) and observed (dashed line) significant wave heights (left) and dominant wave periods (right) at buoys in zone 3 (water depth >200 m).

5. Conclusions

Compared to the conventional SWAN formulation, FVCOM-SWAVE provides an alternative version of the wave model based on an unstructured-grid finite-volume approach. In particular the latter is more suitable for application in coastal and estuarine regions characterized with irregular coastal geometry. Four idealized benchmark test problems in rectangular domains are used to demonstrate that the second-order unstructured-grid finite-volume method used in FVCOM-SWAVE has the same level of accuracy as the third-order finite-difference method used in SWAN. At a fourth test, fetch-limited growth curve analysis following SWAMP Group (1985) shows that FVCOM-SWAVE behaves acceptably in comparison to SWAN growth curves. Finally, an application of the models to the Northwest Atlantic, particularly the Gulf of Maine and related US northeast coastal waters, suggests that FVCOM-SWAVE is robust and can capture the temporal and spatial variation of waves generated by Nor'easters and other high-wind events over both continental shelf and near-shore regions.

Our experiments indicate that the default parameterizations of SWAN (which is adopted by FVCOM-SWAVE) tend to underestimate the significant wave heights during strong wind events. Similar problems were also reported in SWAN's application by Rogers et al. (2002), who found that SWAN tended to underpredict low- and medium-frequency energy in a wind-sea portion of the spectrum. The accuracy of the SWAN simulation is directly affected by parameterization of whitecapping dissipation, as well as nonlinear wave-wave interactions, which are central to the growth and development of wind-generated waves (Zhang et al., 2006; Zhang and Perrie, 2008). The drag coefficient parameterization for surface wind stress is somewhat old, dating from more than 25 years ago. In the current version of SWAN, the surface wind stress is calculated by an empirical function. This function does not capture the wave-age dependence advocated in modern parameterizations for wave drag (Zhang and Perrie, 2008). It is well known that physical processes in wave models have definite limitations, particularly the DIA formulation for nonlinear wave-wave interactions. Resio and Perrie (2008) pointed out very definite problems in simulating shallow water waves, which are the focus for our present paper. Wind input (S_{in}) and dissipation (S_{ds}) are usually tuned to compensate whatever DIA tries to give. This approach, however, cannot compensate for deficiencies in shallow water simulations. Wave-current interaction also may be a factor that can influence wave evolution. These issues are being addressed in our ongoing validation of FVCOM-SWAVE.

The development of advanced inundation and wave forecast system has received increased attention in recent years due to high-wave events combined with massive flooding (e.g., New Orleans during Hurricane Katrina in 2005) and other recent major coastal flooding events where waves were high. Accurate simulation of the wind-driven surface waves is required for the reliable prediction of storm surge processes. In order to set up an accurate reliable forecast system for surface waves using FVCOM-SWAVE, new formulations for the source terms must be developed and implemented in the model. Candidates for these new parameterizations are emerging in recent years (Resio and Perrie, 2008; Perrie and Resio, 2008) and we hope to make appropriate tests with a large number of severe storms. These validation experiments should include a large selection of different wind regimes to validate the accuracy, reliability and limitation of the model for coastal applications.

Acknowledgement

The development of FVCOM-SWAVE was supported by the Massachusetts Marine Fisheries Institute (MFI) (DOC/NOAA/NA04NMF4720332 and DOC/NOAA/NA05NMF4721131), the NOAA NERAC-

OOS Program, NSF projects (OCE0234545, OCE0606928, OCE0712903, OCE0732084 and OCE0726851) and MIT Sea Grant project (NA06OAR41700019). Support also comes from the Canadian Panel on Energy Research and Development (PERD) and GoMOOS – the Gulf of Maine Ocean Observing System.

Appendix A. Discretization of the action density equation in geographic space

The time integration equation of action density in geographic space (Eq. (5) in the text) is rewritten here as

$$\frac{N^{n+\frac{3}{4}} - N^{n+\frac{1}{4}}}{\Delta t} + \nabla \cdot (\bar{C}N) = 0 \quad (A1)$$

where $\bar{C} = \bar{C}_g + \bar{V}$. Integrating (A1) in the control area Ω (see Fig. 1) yields

$$N^{n+\frac{3}{4}} = N^{n+\frac{1}{4}} - \frac{\Delta t}{\Omega} \oint_{\Omega} \nabla \cdot (\bar{C}N) d\Omega = N^{n+\frac{1}{4}} - \frac{\Delta t}{\Omega} \oint_{\Omega} C_n N_l dl. \quad (A2)$$

In the second-order approximated upwind scheme,

$$N_l = \begin{cases} N_{IA} & \text{for } C_n > 0 \\ N_{IB} & \text{for } C_n < 0 \end{cases} \quad (A3)$$

where

$$N_{IA} = N_A + \nabla \cdot N_A \Delta r_A \quad (A4)$$

$$N_{IB} = N_B + \nabla \cdot N_B \Delta r_B. \quad (A5)$$

Integrating (A4) in area Ω_A (a sum of the areas of the light gray triangles), we have

$$N_{IA} = N_A + \frac{\Delta r_A}{\Omega_A} \oint_{\Omega_A} \nabla \cdot N_A d\Omega_A = N_A + \frac{\Delta r_A}{\Omega_A} \oint_{\Omega_A} N_{l\Omega_A} dl_{\Omega_A}. \quad (A6)$$

Similarly, integrating (A5) in area Ω_B (a sum of the areas of triangles with edges shown in dashed line, we have,

$$N_{IB} = N_B + \frac{\Delta r_B}{\Omega_B} \oint_{\Omega_B} \nabla \cdot N_B d\Omega_B = N_B + \frac{\Delta r_B}{\Omega_B} \oint_{\Omega_B} N_{l\Omega_B} dl_{\Omega_B} \quad (A7)$$

The finite-volume discrete expressions of (A2), (A6) and (A7) can be written in the flux form as

$$N^{n+\frac{3}{4}} = N^{n+\frac{1}{4}} - \frac{\Delta t}{\Omega} \sum_{i=1}^{I_n} C_{n,i} N_{l_i} \Delta l_i \quad (A8)$$

$$N_{IA} = N_A + \frac{\Delta r_A}{\Omega_A} \sum_{j=1}^{I_{\Omega_A,n}} N_{l_{\Omega_A,j}} \Delta l_{\Omega_A,j} \quad (A9)$$

$$N_{IB} = N_B + \frac{\Delta r_B}{\Omega_B} \sum_{j=1}^{I_{\Omega_B,n}} N_{l_{\Omega_B,j}} \Delta l_{\Omega_B,j}. \quad (A10)$$

In the explicit scheme, N_l is given by its value at the $(n + 2/4)$ th time step, while in the implicit scheme, it is an unknown variable at the $(n + 3/4)$ th time step.

References

- Battjes, J.A., Janssen, J.P.F.M. 1978. Energy loss and set-up due to breaking of random waves, Proc. 16th Int. Conf. Coastal Engineering, ASCE, pp. 569–587.
- Balay, S., Buschelman, K., Eijkhout, V., Gropp, W., Kaushik, D., Knepley, M., McInnes, L.C., Smith, B., Zhang, H. 2007. PETSc Users Manual. Technical Report ANL-95/11-Revision 2.3.3, Argonne National Laboratory.
- Booij, N., Ris, R.C., Holthuijsen, L.H., 1999. A third-generation wave model for coastal regions, Part I, Model description and validation. J. Geophys. Res. 104 (C4), 7649–7666.
- Boris, J.P., Book, D.L., 1973. Flux corrected transport I, SHASTA, a fluid transport algorithm that works. J. Comp. Phys. 11, 38–69.

- Casulli, V., Lang, G., 2004. Mathematical model UnTRIM, validation document, version June 2004 (1.0). Technical report, Federal Waterways Engineering and Research Institute, Wedeler Landstr. 157, D-22559 Hamburg, pp. 78.
- Cavaleri, L., Malanotte-Rizzoli, P., 1981. Wind wave prediction in shallow water: Theory and application. *J. Geophys. Res.* 86 (C11), 10961–10973.
- Chen, C., Liu, H., Beardsley, R.C., 2003. An unstructured, finite volume, three-dimensional, primitive equation ocean model: Application to coastal ocean and estuaries. *J. Atmos. Oceanic Technol.* 20, 159–186.
- Chen, C., Beardsley, R.C., Cowles, G., 2006a. An unstructured grid, finite-volume coastal ocean model (FVCOM) system. Special Issue entitled "Advances in Computational Oceanography". *Oceanography*, 19(1), 78–89.
- Chen, C., Beardsley, R.C., Cowles, G., 2006b. An unstructured grid, finite-volume coastal ocean model FVCOM user manual. SMASST/UMASSD, 2006.
- Chen, C., Huang, H., Beardsley, R.C., Liu, H., Xu, Q., Cowles, G., 2007. A finite-volume numerical approach for coastal ocean circulation studies: comparisons with finite difference models. *J. Geophys. Res.* 112, C03018. doi:10.1029/2006JC003485.
- Collins, J.I., 1972. Prediction of shallow water spectra. *J. Geophys. Res.* 77 (15), 2693–2707.
- Cowles, G., 2008. Parallelization of the FVCOM Coastal Ocean Model. *International Journal of High Performance Computing Applications* 22 (2), 177–193.
- Crank, J., Nicolson, P., 1947. A practical method for numerical evaluation of partial differential equations of the heat conduction type. *Proceedings of the Cambridge Philosophical Society* 43, 50–64.
- Eldeberky, Y., 1996. Nonlinear transformation of wave spectra in the nearshore zone. Ph.D. thesis, Delft University of Technology, Department of Civil Engineering, The Netherlands.
- Fringer, O.B., Gerritsen, M., Street, R.L., 2006. An unstructured-grid, finite-volume, nonhydrostatic, parallel coastal ocean simulator. *Ocean Modelling* 14, 139–173.
- Hasselmann, K., 1974. On the spectral dissipation of ocean waves due to whitecapping. *Bound.-layer Meteor.* 6 (1–2), 107–127.
- Hasselmann, S., Hasselmann, K., Allender, J.H., Barnett, T.P., 1985. Computations and parameterizations of the nonlinear energy transfer in a gravity wave spectrum. Part II: Parameterizations of the nonlinear transfer for application in wave models. *J. Phys. Oceanogr.* 15, 1378–1391.
- Hsu, T., Ou, S., Liau, J., 2005. Hindcasting nearshore wind waves using a FEM code for SWAN. *Coastal Engineering* 52, 177–195.
- HYPRE Team (2001), HYPRE-high performance preconditions, user's manual. Center for Applied Scientific Computing, Lawrence Livermore National Laboratory, 48pp.
- Komen, G.J., Hasselmann, S., Hasselmann, K., 1984. On the existence of a fully developed wind-sea spectrum. *J. Phys. Oceanogr.* 14, 1271–1285.
- Lai, Z., Chen, C., Cowles, G., Beardsley, R.C., 2008. A non-hydrostatic version of FVCOM-validation experiment I: surface standing and solitary waves. *J. Geophys. Res.*, submitted.
- Madsen, O.S., Poon, Y.-K., Graber, H.C., 1988. Spectral wave attenuation by bottom friction: Theory. *Proc. 21th Int. Conf. Coastal Engineering*, ASCE, 492–504.
- Perrie, W., Resio, D., 2008. A two-scale approximation for efficient representation of nonlinear energy transfers in a wind wave spectrum. Part 2 Application to observed wave spectra. Submitted to *J. Phys. Oceanogr.*
- Pierson, W.J., Moskowitz, L., 1964. A proposed spectral form for fully developed wind seas based on the similarity theory of S.A. Kitaigorodskii. *J. Geophys. Res.* 69 (24), 5181–5190.
- Resio, D., Perrie, W., 2008. A two-scale approximation for efficient representation of nonlinear energy transfers in a wind wave spectrum. Part 1: Theoretical Development. *J. Phys. Oceanogr.* 38 (12), 2801–2816.
- Rogers, W.E., Kaihatu, J.M., Petit, H.A.H., Booij, N., Holthuijsen, L.H., 2002. Diffusion reduction in an arbitrary scale third generation wind wave model. *Ocean Engng.* 29, 1357–1390.
- SWAMP Group. 1985. *Ocean Wave Modelling*. Plenum, New York, 256 pp.
- SWAN Team. 2006a. SWAN Cycle III version 40.51 Technical documentation. Delft University of Technology, Faculty of Civil Engineering and Geosciences, Environmental Fluid Mechanics Section, P.O.Box 5048, 2600 GA Delft, The Netherlands.
- SWAN Team. 2006b. SWAN Cycle III version 40.51 user manual. Delft University of Technology, Faculty of Civil Engineering and Geosciences, Environmental Fluid Mechanics Section, P.O. Box 5048, 2600 GA Delft, The Netherlands.
- Tolman, H.L. 2002. User manual and system documentation of WAVEWATCH-III version 2.22. Environmental Modeling Center, Marine Modeling and Analysis Branch, NOAA.
- WAMDI Group. 1988. The WAM model – A third generation ocean wave prediction model. *J. Phys. Oceanogr.* 18, 1775–1810.
- Wu, J., 1982. Wind-stress coefficients over sea surface from breeze to hurricane. *J. Geophys. Res.* C87, 9704–9706. doi:10.1029/JC087iC12p09704.
- Zhang, W., Perrie, W., 2008. The influence of air-sea roughness, sea spray and storm translation speed on waves. *J. Physical Oceanogr.* 38 (4), 817–839.
- Zhang, W., Perrie, W., Li, W., 2006. Impacts of waves and sea spray on mid-latitude storm structure and intensity. *Monthly Weather Review* 134 (9), 2418–2442.